

1 **Time-resolved dynamic optical coherence tomography for retinal** 2 **blood flow analysis**

3 Philippe Valmaggia^{1,2,3}, Philippe C. Cattin¹, Robin Sandkühler¹, Nadja Inglin²,
4 Tilman P. Otto⁴, Silke Aumann⁴, Michel M. Teussink⁴, Richard F. Spaide⁵,
5 Hendrik P. N. Scholl^{2,3}, Peter M. Maloca^{2,3}

6 ¹Department of Biomedical Engineering, University of Basel, 4123 Allschwil,
7 Switzerland

8 ²Institute of Molecular and Clinical Ophthalmology Basel (IOB), Basel, 4031 Basel,
9 Switzerland

10 ³Department of Ophthalmology, University Hospital Basel, 4031 Basel, Switzerland

11 ⁴Heidelberg Engineering GmbH, 69115 Heidelberg, Germany

12 ⁵Vitreous Retina Macula Consultants of New York, NY 10022, USA

13

14 **Word count:** Abstract: 245; Manuscript: 4'218

15 **Corresponding author:** Philippe Valmaggia, Department of Biomedical
16 Engineering, University of Basel, 4123 Allschwil, Switzerland. Email:
17 philippe.valmaggia@unibas.ch

18 **Keywords:** time-resolved, dynamic, optical coherence tomography, retinal blood
19 flow, flow velocity

20 **Commercial relationships:** PV received funding from the Swiss National Science
21 Foundation (Grant 323530_199395), the Janggen-Pöhn Stiftung and AlumniMedizin
22 Basel and discloses personal compensation from Heidelberg Engineering GmbH.
23 TPO, SA and MMT are salaried employees of Heidelberg Engineering GmbH, 69115
24 Heidelberg, Germany. RFS discloses personal compensation from Topcon Medical
25 Systems, Roche, Bayer, Heidelberg Engineering and Genentech. HPNS is
26 supported by the Swiss National Science Foundation (Project funding: “Developing
27 novel outcomes for clinical trials in Stargardt disease using structure/function
28 relationship and deep learning” #310030_201165, and National Center of
29 Competence in Research Molecular Systems Engineering: “NCCR MSE: Molecular
30 Systems Engineering (phase II)” #51NF40-182895), the Wellcome Trust (PINNACLE
31 study), and the Foundation Fighting Blindness Clinical Research Institute (ProgStar
32 study). HPNS is a member of the Scientific Advisory Board of Boehringer Ingelheim
33 Pharma GmbH & Co; Claris Biotherapeutics Inc.; Eluminex Biosciences; Gyroscope
34 Therapeutics Ltd.; Janssen Research & Development, LLC (Johnson & Johnson);
35 Novartis Pharma AG (CORE); Okuvision GmbH; ReVision Therapeutics Inc.; and
36 Saliogen Therapeutics Inc. HPNS is a consultant of: Alnylam Pharmaceuticals Inc.;
37 Gerson Lehrman Group Inc.; Guidepoint Global, LLC; and Intergalactic Therapeutics
38 Inc. HPNS is member of the Data Monitoring and Safety Board/Committee of Belite
39 Bio (CT2019-CTN-04690-1), F. Hoffmann-La Roche Ltd (VELODROME trial,
40 NCT04657289; DIAGRID trial, NCT05126966; HUTONG trial) and member of the
41 Steering Committee of Novo Nordisk (FOCUS trial; NCT03811561). All
42 arrangements have been reviewed and approved by the University of Basel
43 (Universitätsspital Basel, USB) and the Board of Directors of the Institute of
44 Molecular and Clinical Ophthalmology Basel (IOB), in accordance with their conflict-
45 of-interest policies. Compensation is being negotiated and administered as grants by
46 USB, which receives them on its proper accounts. HPNS is co-director of the
47 Institute of Molecular and Clinical Ophthalmology Basel (IOB), which is constituted
48 as a non-profit foundation and receives funding from the University of Basel, the
49 University Hospital Basel, Novartis and the government of Basel-Stadt. PMM is a
50 consultant of Roche and holds intellectual properties for machine learning at MIMO
51 AG and VisionAI, Switzerland. Funding organisations had no influence on the
52 design, performance or evaluation of the current study. The other authors declare no
53 conflict.

54 **Abstract**

55 **Purpose:** Optical coherence tomography (OCT) representations in clinical practice
56 are static and do not allow for a dynamic visualisation and quantification of blood
57 flow. This study aims to present a method to analyse retinal blood flow dynamics
58 using time-resolved structural optical coherence tomography (OCT).

59 **Methods:** We developed novel imaging protocols to acquire video-rate time-resolved
60 OCT B-scans (1024 x 496 pixels, 10° field of view) at four different sensor integration
61 times (integration time of 44.8 μ s at a nominal A-scan rate of 20 kHz, 22.4 μ s at 40
62 kHz, 11.2 μ s at 85 kHz, 7.24 μ s at 125 kHz). The vessel centres were manually
63 annotated for each B-scan and surrounding subvolumes were extracted. We used a
64 velocity model based on signal-to-noise ratio (SNR) drops due to fringe washout to
65 calculate blood flow velocity profiles in vessels within five optic disc diameters of the
66 optic disc rim.

67 **Results:** Time-resolved dynamic structural OCT revealed pulsatile SNR changes in
68 the analysed vessels and allowed the calculation of potential blood flow velocities at
69 all integration times. Fringe washout was stronger in acquisitions with longer
70 integration times; however, the ratio of the average SNR to the peak SNR inside the
71 vessel was similar across all integration times.

72 **Conclusions:** We demonstrated the feasibility of estimating blood flow profiles
73 based on fringe washout analysis, showing pulsatile dynamics in vessels close to the
74 optic nerve head using structural OCT. Time-resolved dynamic OCT has the
75 potential to uncover valuable blood flow information in clinical settings.

76 **Introduction**

77 Optical coherence tomography (OCT) is a technology that enables the visualisation
78 of retinal structures on a micrometre scale.^{1,2} Its benefits of being non-invasive, fast
79 and easy to operate have made OCT become one of the most widely used imaging
80 techniques, particularly in ophthalmology.³ Since its first demonstration in 1991, OCT
81 has been enhanced and nowadays, allows the visualisation of intravascular flow
82 regions through OCT angiography (OCTA).⁴ OCTA is based on the detection of OCT
83 signal changes over time and allows the visualisation of chorioretinal vasculature
84 down to the microvasculature in an unprecedented way.

85 However, the clinical representations of both OCT and OCTA are static. For
86 visualising flow dynamics and analysing changes within single vessels over time,
87 ophthalmologists and researchers must rely on other acquisition modalities such as
88 Doppler OCT, laser speckle flowgraphy, the retinal function imager or variable
89 interscan time analysis (VISTA) in macular OCTA.⁵⁻¹³ These techniques are mostly
90 used in specialised research centres and are not yet widely used in everyday clinical
91 use. Due to the relatively high demands on technology and experience, they have
92 not yet been implemented in a routine clinical application that can be used on a daily
93 basis. However, the scan patterns in OCT devices are generally customisable and
94 modifications would allow for dynamic acquisitions and visualisations in clinical
95 settings. Sequentially acquired OCT signals at the same position particularly
96 fluctuate within and in close proximity to vessels; accordingly, they have the greatest
97 contribution to OCTA signal generation.^{4,14}

98 The OCT signals are generated by measuring the interference pattern of reflected
99 light waves from a sample and a reference mirror.^{1,15,16} The reflected light waves
100 interfere constructively or destructively, generating interference patterns of light and

101 dark bands which are called interference fringes^{15,17} – appearing similar to the edge
102 of a fabric fringe. When the sample or instrument moves during image acquisition,
103 the phase of the reflected light changes. This modulation of the interference can
104 cause the interference fringes to vanish, a phenomenon called fringe washout. The
105 fringe washout leads to a signal-to-noise ratio (SNR) drop in the image, which tends
106 to be larger in case of a larger sample motion.^{18–20} This can occur at higher sample
107 velocities or increased sensor integration times.¹⁸ Taking advantage of the
108 knowledge that fringe washout is directly linked to the velocity of the sample motion,
109 we investigated the possibility of calculating flow profiles in time-resolved structural
110 OCT data. An overview of the general principle of fringe washout can be found in
111 Figure 1.

112 To investigate blood flow velocity, we modified the OCT scan patterns of a
113 commercially available device to allow for time-resolved dynamic acquisitions.
114 Furthermore, we analysed these images regarding the fringe washout and present
115 dynamically calculated blood flow profiles.

116 **Methods**

117 **Data acquisition**

118 Data were acquired at the Augenarztpraxis Dr. Maloca in Lucerne, Switzerland. The
119 study was performed according to the Declaration of Helsinki, and ethics approval
120 was granted by the Ethics Committee of Northwestern and Central Switzerland
121 (EKNZ 2021-02360). Written informed consent was obtained from all participants.

122 The images were acquired with a Heidelberg Spectralis OCT with an investigational
123 acquisition module. The OCT volume acquisition pattern was modified to continuous
124 B-scans with a 10° field of view without OCT tracking through the on-board dual-
125 beam confocal scanning laser ophthalmoscope tracking system. This prevented
126 irregular OCT B-scan acquisition due to compensatory OCT-beam steering by the
127 tracking system, which has a variable time lag. The patients were informed about the
128 acquisition procedure to ensure good image quality. The subjects were instructed to
129 fixate on the foveal fixation target, close their eyes, blink once and then leave their
130 eyes open. Acquisitions were performed for several seconds, where a manual press
131 on the joystick of the OCT device allowed to start and end the acquisition. In the
132 case of blinks or major ocular movements, the process was repeated.

133 The acquisitions were performed between the optic nerve head centre and five optic
134 disc diameters (ODDs) from the optic nerve rim and graded by eccentricity 0–6 (0:
135 optic nerve head centre, 1: neuroretinal rim, 2: 1 ODD superotemporal to the
136 neuroretinal rim, 3: 2 ODDs, 4: 3 ODDs, 5: 4 ODDs, 6: 5 ODDs). The major visible
137 vessels were imaged perpendicularly, so that the cross-section was visible.

138 All time-resolved acquisitions were performed with continuous B-scans, each single
139 scan comprising 1024 A-scans with 496 pixels, with a 10° field of view. This allowed

140 the same B-scan to be repeated at the same location with a high sampling density
141 over a longer period of time and still meet the requirements regarding light safety. All
142 locations were acquired at four different A-scan integration times 44.8, 22.4, 11.2
143 and 7.24 μ s, corresponding to nominal A-scan rates of 20, 40, 85 and 125 kHz,
144 respectively. This enabled video-rate sequential B-scan acquisitions. Each separate
145 B-scan was saved as a single image without averaging. Notably, the SNR in
146 spectral-domain (SD) OCTs depends on the integration time according to the
147 following established formula^{21–23}:

$$148 \quad SNR_{SD} \sim (\eta * P_{sample} * \tau_i) / E_v,$$

149 where η corresponds to the spectrometer efficiency, P_{sample} to the power returned in
150 the sample arm, τ_i to the integration time and E_v to the energy per photon. A
151 validation of this formula was investigated during this in vivo study. The SNR for
152 each individual B-scan was calculated with the raw data by the ratio of the maximum
153 intensity to the noise level. Overall, the SNR values were compared for each
154 integration time.

155 **Image processing**

156 All image stacks were exported from the OCT device in normalised raw format (.vol
157 files, image intensities normalised between 0 and 1 at a B-scan level). In the first
158 step, all image stacks were transformed for a visual representation by multiplying all
159 image intensities by 255 times the 4th square root of the normalised intensity. These
160 transformed images stacks were then registered using a rigid body transformation
161 model with a pyramid processing scheme.²⁴ This registration pipeline was adapted to
162 reduce the effect of speckle noise in the registration process. The mean of the first
163 10 images of the image stack was used as the reference image for the registration of

164 the complete image stack. Rigid body registration was applied to prevent distortion of
165 the retina and to allow visualisation of the time-resolved B-scan stack. In the second
166 step, the vessel centres of prominently visible vessels were manually annotated, and
167 subvolumes of 7×7 pixels around the centre were extracted from each B-scan. This
168 subvolume corresponded to physical dimensions of $20 \mu\text{m}$ along the B-scan axis and
169 $27 \mu\text{m}$ along the A-scan axis.

170 In a second step, the extracted subvolumes were analysed with their original, non-
171 normalised intensities, which were obtained from the metadata of the .vol files. The
172 SNR in the individual vessel subvolumes were then calculated as the ratio of the
173 average pixel intensity in the subvolume to the noise level of the B-scan, assuming
174 shot noise limited detection. The noise level of the B-scan was approximated using
175 the Heidelberg Quality score (in dB) and the maximum intensity value of the B-Scan.
176 A depth-specific noise level to account for roll-off was not obtainable with the present
177 data. An overview of the main image processing steps is shown in Figure 2.

178 **Flow profile generation**

179 Fringe washout is a phenomenon occurring when imaged particles are moving which
180 leads to a SNR drop in the OCT image. The effect is linked to the integration time
181 and is attributed to the modulation of the interference signal when particles are in
182 motion. Typically, the fringe washout is more pronounced as the integration time
183 increases. Yun et al. presented formulas for the fringe washout describing separately
184 the axial and lateral components of particle movements.¹⁸ In the case of oblique
185 motion, the axial component is orders of magnitude larger when compared with the
186 lateral component.¹⁹ In this work, we used the squared sinc function presented for
187 the axial component of the fringe washout to calculate blood flow velocity profiles¹⁸:

188 $SNR_{Drop} = \sin(k_0 \Delta z)^2 / (k_0 \Delta z)^2,$

189 where $k_0 = 2\pi / \lambda$ and $\Delta z = n * v * \tau$. k_0 corresponds to the central wavenumber of
190 the light source, λ to the central wavelength of the light source, Δz to the
191 displacement in the z-axis, n to the refractive index of the eye, τ to the integration
192 time, and v to the velocity.

193 This quadratic sinc function, with a known SNR drop, was solved numerically for
194 velocity. All numerical solutions per B-scan were stored as a potential flow velocity.
195 The results of the equation for each B-scan, SNR_{Drop} , were used to generate the
196 dynamic flow profiles. Figure 3 presents the SNR_{Drop} profiles at the four acquisition
197 rates with calculated velocities in mm/s for any moving object. For this study, the
198 average SNR of the 7×7 B-scan subvolume was divided by the maximum SNR at
199 the pixel level of the complete vessel subvolume ($7 \times 7 \times$ number of B-scans) to
200 calculate the SNR_{Drop} . All calculations were made with absolute SNR values. The
201 calculated velocities are presented in arbitrary units since the formula only takes into
202 account the axial component and the SNR inside the vessels without flow, which
203 would be the reference for SNR_{Drop} calculations, could not be determined.

204 **Data analysis**

205 The generated flow profiles were quantitatively and qualitatively analysed. On a
206 qualitative level, the generated dynamic OCTs and the course of the pulse waves
207 were analysed. The quantitative analysis was focused on the flow profiles, where the
208 minimal, maximal, and average velocities for each vessel at each B-scan were
209 calculated. The minimal velocity refers to the smallest numerical solution of the
210 SNR_{Drop} equation, the maximum velocity refers to the largest solution, and the
211 average velocity refers to the average of all numerical solutions per B-scan.

212 Furthermore, the exam duration, the SNR of the B-scans, the mean and maximal
213 intensity of the subvolumes, and the maximum image intensity in the raw data were
214 analysed. Programming was performed with Linux shell scripts, Python 3.9 (Python
215 Software Foundation, Wilmington, USA) and R V4.2.2 (Foundation for Statistical
216 Computing, Vienna, Austria). The data were visualised with Python 3.9, R V4.2.2
217 and 3DSlicer V4.11.^{25,26}

218 **Results**

219 A total of 164 time-resolved image stacks from six healthy subjects were acquired
220 and manually annotated. All acquisitions were performed in the right eyes of the
221 patients. The image stacks consisted of 47 to 483 B-scans, and between 1 and 5
222 vessels were annotated per volume. In summary, 466 vessels were annotated in the
223 time-series data, totalling 94,619 annotated vessel centres.

224 **Qualitative analysis**

225 Time-resolved dynamic acquisitions of structural OCT are feasible in healthy
226 subjects and show changes in reconstructed images over time. These changes are
227 of different nature, where pulsatile profiles can be clearly identified. Supplementary
228 Video 1 shows the pulsation inside an artery at the centre of the optic nerve as
229 changes in image intensity. Furthermore, we can see pulsation of the optic nerve
230 head tissue. Supplementary Video 2 shows a longitudinal cut through the same
231 artery, where we can observe the fringe washout along the vessel. We detected an
232 increase in the fringe washout at the centre of the vessel, showing a higher relative
233 flow velocity. In addition, we identified a bimodal peak of the fringe washout.

234 Qualitative analysis of the generated flow profiles confirmed this pulsatility for the
235 SNR changes and the calculated flow velocities. As depicted for an acquisition at the
236 optic nerve head centre in Figure 4, the flow profiles show pulsatility where maximal
237 and minimal velocities were clearly distinguishable. In addition, the flow velocities
238 showed a rapid increase, followed by a gradual decrease towards a steady-state
239 until the pulsatile cycle restarted. As shown in Figure 5, this flow profile could be
240 visualised at all four acquisition rates, with a constant repetition of approximately four
241 pulse visualisations within 3 s. These observations suggest that the pulsation

242 propagates in correspondence with the cardiac cycle, which corresponds in this
243 example to a heart rate of 80 beats per minute.

244 When analysing the blood flow profiles at different eccentricities, pulsatility was
245 evident close to the optic nerve centre. The pulsatility decreased towards the
246 periphery, where a distinct change tended to occur when the vessel crossed the
247 optic nerve head rim. Figure 6 provides a visual representation of this finding by
248 showing the calculated blood flow profiles along with an en-face representation of
249 their acquisition location. Further, we observed a decrease of the estimated average
250 flow velocity towards the periphery, here again with an apparent decrease at the
251 crossing of the vessel of the optic nerve head rim.

252 **Quantitative analysis**

253 We validated whether the SNR variability inside the vessels was different from the
254 SNR variability in adjacent tissue, as the fringe washout variability could occur due to
255 axial bulk motion. For this analysis, we annotated further retinal nerve fibre layer
256 (RNFL) subvolumes in the proximity of an artery as the RNFL is known to have a
257 high reflectivity in OCT.²⁷ We analysed the SNR in the vessel (SNR_{vessel}), the SNR in
258 the RNFL (SNR_{RNFL}) and the SNR in the complete B-scan ($SNR_{\text{B-scan}}$). The analysis
259 confirmed that the SNR_{vessel} was lower than the SNR_{RNFL} . The $SNR_{\text{B-scan}}$ was the
260 highest as it was defined by the peak SNR in the complete image. The $SNR_{\text{vessel}} /$
261 $SNR_{\text{B-scan}}$ ratio vessel clearly decreased with longer integration times while the
262 $SNR_{\text{RNFL}} / SNR_{\text{B-scan}}$ ratio showed less variability. This showed that the fringe
263 washout inside the vessels was stronger at longer integration times. The SNR
264 comparison of the artery and the RNFL are further described for the different
265 integration times in Table 1. A visualisation of the fringe washout at the different

266 integration times can be found in the Supplementary Video 3, where the SNR drops
267 diminish with faster acquisitions.

268 An overview of the statistics and the calculated velocities per A-scan rate can be
269 found in Tables 2 and 3. When analysing the absolute SNRs, $SNR_{B\text{-scan}}$ and
270 SNR_{Vessel} correlated with integration time. The calculated factors of the integration
271 times of 44.8 μs at a nominal A-scan rate of 20 kHz, 22.4 μs at 40 kHz 11.2 μs at 85
272 kHz, 7.24 μs at 125 kHz are 6.19, 3.09, and 1.55 to 1 when taking the shortest
273 integration time as a reference. Median $SNR_{B\text{-scan}}$ factors are 5.83, 3.73, and 1.75 to
274 1, respectively. In summary, a longer integration time led to an increase of both
275 absolute SNR_{Vessel} and $SNR_{B\text{-scan}}$, and a decrease of the $SNR_{Vessel} / SNR_{B\text{-scan}}$ ratio.
276 This is also shown in the $SNR_{Subvolume} / SNR_{B\text{-scan}}$ for the arteries in Table 1.

277 The $SNR_{Vessel} / \text{Peak } SNR_{Vessel}$ ratio corresponds to the SNR drop with which the flow
278 velocities were calculated. This ratio remained constant across the varying
279 integration times. Given that Yun et al.'s model for flow velocities is dependent on
280 the integration time, the calculated flow velocities showed a linear relationship with
281 their integration time ratio.¹⁸ In the analysis of the flow velocities at different
282 distances from the optic nerve head of the complete cohort, decreasing calculated
283 mean flow velocity along the vessel arch were observed. A summary overview of the
284 flow velocities along the vessel arch is shown in Figure 7, with corresponding
285 examples of SLOs.

286 Discussion

287 To analyse the dynamics within retinal structures and, more specifically, in vessels,
288 we developed acquisition protocols for dynamic time-resolved OCT measurements
289 utilising a commercially available OCT device widely used in clinics. Taking
290 advantage of the fringe washout phenomenon of spectral-domain OCTs, we
291 calculated time-resolved velocity profiles based on the SNR drop within the vessels.
292 In addition, we found pulsatile blood flow profiles, where the amplitude and average
293 velocity decreased from the centre of the optic nerve head towards the retinal
294 periphery.

295 This study presents several novel possibilities for the analysis of OCT data acquired
296 with a commercially available device. First, time-resolved dynamic OCT with a
297 matching of B-scans to a time axis allowed us to assess structural changes with an
298 interval of as low as 9 ms between B-scans. The matching of the B-scans to a time
299 axis allowed for generating videos with real interframe intervals (Supplementary
300 Videos 1 and 2). Considering that inter-B-scan intervals differ when tracking is
301 activated and individual B-scans are averaged, continuous visualisations of B-scans
302 can create an incorrect impression of the speed at which changes happen.

303 Second, this study presents methods for comparing OCT acquisitions with different
304 integration times. As OCT phenomena, such as the fringe washout, are affected by
305 the integration time, it is important to consider parameters such as the image quality
306 or the OCT intensity, which vary with different integration times.^{18,28} In this study, we
307 showed in vivo that the fringe washout phenomenon varies for different integration
308 times. The fringe washout in vessels was stronger at longer integration times, which
309 should be considered in further studies.

310 Third, we combined this knowledge to investigate and visualise pulsatile dynamics
311 within vessels in structural OCT. For this, we took advantage of the fact that the
312 fringe washout analysis allows for the calculation of corresponding flow velocities.
313 We generated blood flow profiles by calculating the flow velocity of the axial motion
314 component for each time-resolved B-scan. OCT is primarily utilised for visualising
315 retinal tissue, but it provides several advantages over OCTA in certain scenarios. In
316 particular, structural OCT allows to directly work with the raw intensities from the
317 acquisition as opposed to post-processed images. As a result, OCT can also be
318 advantageous for the analysis of vessels, as it provides direct information about the
319 characteristics of the tissue being imaged.

320 The analysis of the fringe washout would generally allow the calculation of velocities
321 in mm/s. However, there are several limitations to quantitative values that we could
322 not address in this work. The fringe washout is composed of axial and lateral
323 components. Weighing both components is possible if the angle of the vessel and
324 sample motion is known.²⁹ However, the axial component is larger by orders of
325 magnitude compared with the lateral component in the case of oblique motion.¹⁹ A
326 further limitation that must be addressed is the reference intensity to calculate the
327 SNR drop, which cannot be determined in a moving system. The optical properties of
328 the eye, such as the clarity of the optical media as the lens, the cornea or even the
329 momentaneous tear film affect the SNR.³⁰ Furthermore, the peak SNR inside a
330 vessel is also affected by fringe washout, as there is permanent motion in a larger
331 vessel in vivo. Hence, an absolute reference value or an external calibration seems
332 difficult to determine, even under ideal circumstances. Further, the sensitivity roll-off
333 along the A-scan axis was not assessed and hence not included in the noise
334 calculations. An analysis of the transformation matrices used in the registration

335 process could assist in calculating the fringe washout component caused by bulk eye
336 motion. In this work, we focused on the analysis of the axial component of the fringe
337 washout to calculate potential blood flow velocities and estimate relative flow profiles
338 in vivo. For this, we calculated numerical solutions to the SNR_{Drop} equation
339 representing potential axial flow velocities. We present estimated flow velocity
340 profiles in arbitrary units as an average of all the numerical solutions per B-Scan. It's
341 important to note that these velocity profiles are estimates as there are multiple
342 numerical solutions to the SNR_{Drop} equation. Potentially, for certain B-scans a lower
343 numerical solution could represent the real velocity, while for others with the same
344 SNR_{Drop} a higher numerical solution would be correct. To determine which numerical
345 solutions to the equation accurately reflect the true axial flow velocity values, further
346 validation of the technique is required.

347 An objective reference value could help align the different flow velocities we found at
348 different acquisition rates by using the formula by Yun et al.¹⁸ The calculated
349 average, minimum and maximum flow velocities seem to be inversely dependent on
350 the integration time as shown in Table 3. Further, we found that the absolute SNR in
351 the vessels increases with increasing integration time, however, that the relative
352 SNR drop within the vessels remained constant across the integration times. The
353 major advantage of this finding is that blood flow profiles can be estimated and
354 visualised independently from the integration time, even at higher acquisition rates
355 where there is less relative fringe washout.

356 The decreasing velocity of the flow profiles along the vessel arch suggest that the
357 method can grasp decreasing velocities in accordance with known physiologic
358 principles. However, this cannot yet be supported by our data as the angle between
359 the beam and the flow direction varies across the retina. Such changes in the angle

360 also affect the axial velocity component. In accordance with this, we noticed that the
361 pulsatility of the calculated blood flow profiles tends to decrease when an artery
362 crosses the optic nerve head rim. For a precise measurement of the flow velocity,
363 again the lateral component or the angle of the vessel would have to be known.²⁹
364 Other techniques to measure retinal blood flow exist, such as Doppler OCT, laser
365 speckle flowgraphy and VISTA in OCTA.^{5,6,8,31} The analysis of retinal blood flow
366 based on intensity changes has also been presented for a neural network-based
367 approach.³² However, these technologies are mainly used in research environments
368 and are not yet regularly in clinical practice as the required phase information or A-
369 scan acquisition rates are not widely available. Our method allows to calculate retinal
370 blood flow velocity profiles with a widely used clinical device while at the same time
371 contributing to bridge the gap left by other measurement techniques. Techniques
372 such as laser Doppler flowmetry can only be used if the Doppler angle is known;
373 laser speckle flowgraphy does not allow for a depth-resolved flow measurement; and
374 VISTA is an extension of OCTA that has been presented for the macular area
375 only.^{8,31} This could be mainly due to the fact that the line rates of the lasers are
376 currently not high enough to measure changes in the saturation of signal changes for
377 VISTA outside the macular area. With further validation, our method could allow the
378 visualisation of depth- and time-resolved flow profiles, as shown in this study for
379 vessels around the optic nerve head. Ideally, our method could be further enhanced
380 by including Doppler angle and phase shift information to translate combined
381 findings into clinical practice.^{5,10,19} A validation of newly obtained blood flow profile
382 values could be achieved by comparing them with measurements from flow
383 phantoms.¹⁹

384 To analyse retinal blood flow is relevant as the vasculature is involved in many
385 ocular diseases, such as diabetic retinopathy and glaucoma. Blood flow
386 disturbances, such as haemorrhage or ischemic attacks, can lead to vision loss and
387 identifying vessels at risk could help prevent vascular injuries. For accurate and
388 easy-to-use measurements, blood flow measurements must be implemented in
389 clinics. We aim to contribute to this goal with the proposed time-resolved structural
390 OCT-generated flow profiles. Thus far, our method has only been tested in healthy
391 participants and not yet in subjects with ocular diseases. The short-term
392 reproducibility for the generation of flow profiles at the same location was good. Very
393 similar flow profiles could be generated during acquisitions with different integration
394 times at the same location. Short-term reproducibility at the same location with the
395 same integration time as well as inter-visit reproducibility and variability still need to
396 be determined. The method could be further validated by imaging subjects with
397 diseases such as glaucoma or diabetic retinopathy, as their blood flow has been
398 shown to be altered with other measuring techniques.^{33–35} The new estimates of
399 retinal blood flow profiles could also be compared against the previously described
400 techniques in further studies.

401 Future work will include a deeper analysis of the pulsatile flow profiles. As shown in
402 Figures 4 and 5 and Supplementary Videos 2 and 3, the pulse wave appeared to
403 have a bimodal peak, which would be congruent with the propagation of the aortic
404 pulse wave.³⁶ In addition, the pulse wave analysis, in combination with absolute
405 velocity and flow information, could also be used to analyse the retinal blood flow
406 volume and parts of the cardiac output arriving at the eye from the heart.^{10,37} An
407 extension of this could also include the investigation of the best acquisition location,
408 differences across branching points and general differences between arteries and

409 veins. The current measurements are consecutive B-scan acquisitions over time,
410 with a minimal inter-B-scan interval of ~9 ms at 1024 A-scans. With fast acquisition
411 speeds and a small number of B-scans, 4D cross-sectional acquisitions can become
412 feasible. Hereby, the pulsatile nature of the fringe washout indicates a correlation
413 with the cardiac cycle and a representation of the pulse propagation in the
414 vasculature of the optic nerve head. In vivo measurements could investigate the
415 validity of models about the pulse propagation towards the eye.³⁸

416

417 **Conclusions**

418 In summary, this study showed that time-resolved OCT acquisitions are feasible in
419 vivo and that continuous acquisitions over several seconds can be made with a
420 widely used clinical device. We showed that dynamic blood flow profiles can be
421 calculated from time-resolved OCT acquisitions. Time-resolved dynamic OCT, with
422 its high spatial and temporal resolution, holds promising information that can be
423 further investigated as a novel clinically applicable parameter for the assessment of
424 retinal blood flow velocity profiles.

425

426 **Acknowledgements**

427 The authors wish to thank the Swiss National Science Foundation, the Janggen-
428 Pöhn-Stiftung and the AlumniMedizin Basel for their financial support of this project.

429 In addition, the researchers would like to thank all the participants who volunteered
430 for this study.

431 References

- 432 1. Huang D, Swanson EA, Lin CP, Schuman JS, Stinson WG, Chang W, Hee MR, Flotte
433 T, Gregory K, Puliafito CA, Fujimoto JG. Optical coherence tomography. *Science*.
434 1991;254(5035):1178-1181. doi:10.1126/science.1957169
- 435 2. Chinn SR, Swanson EA, Fujimoto JG. Optical coherence tomography using a
436 frequency-tunable optical source. *Opt Lett*. 1997;22(5):340. doi:10.1364/ol.22.000340
- 437 3. Fujimoto J, Swanson E. The development, commercialization, and impact of optical
438 coherence tomography. *Investig Ophthalmol Vis Sci*. 2016;57(9):OCT1-OCT13.
439 doi:10.1167/iovs.16-19963
- 440 4. Spaide RF, Fujimoto JG, Waheed NK, Sadda SR, Staurengi G. Optical coherence
441 tomography angiography. *Prog Retin Eye Res*. 2018;64:1-55.
442 doi:10.1016/j.preteyeres.2017.11.003
- 443 5. Leitgeb RA, Werkmeister RM, Blatter C, Schmetterer L. Doppler Optical Coherence
444 Tomography. *Prog Retin Eye Res*. 2014;41:26-43.
445 doi:10.1016/j.preteyeres.2014.03.004
- 446 6. Sugiyama T. Basic technology and clinical applications of the updated model of laser
447 speckle flowgraphy to ocular diseases. *Photonics*. 2014;1(3):220-234.
448 doi:10.3390/photonics1030220
- 449 7. Wang L, Jiang H, Grinvald A, Jayadev C, Wang J. A Mini Review of Clinical and
450 Research Applications of the Retinal Function Imager. *Curr Eye Res*. 2018;43(3):273-
451 288. doi:10.1080/02713683.2017.1414853
- 452 8. Ploner SB, Moulton EM, Choi W, Waheed NK, Lee B, Novais EA, Cole ED, Potsaid B,
453 Husvogt L, Schottenhamml J, Maier A, Rosenfeld PJ, Duker JS, Hornegger J,
454 Fujimoto JG. Toward quantitative optical coherence tomography angiography:
455 Visualizing blood flow speeds in ocular: Pathology using variable interscan time
456 analysis. In: *Retina*. Vol 36. NIH Public Access; 2016:S118-S126.
457 doi:10.1097/IAE.0000000000001328
- 458 9. White BR, Nassif N, Boer JF de, Cense B, Bouma BE, Park BH, Chen TC, Tearney
459 GJ, Pierce MC. In vivo dynamic human retinal blood flow imaging using ultra-high-
460 speed spectral domain optical Doppler tomography. *Opt Express*, Vol 11, Issue 25, pp
461 3490-3497. 2003;11(25):3490-3497. doi:10.1364/OE.11.003490
- 462 10. Baumann B, Potsaid B, Kraus MF, Liu JJ, Huang D, Hornegger J, Cable AE, Duker
463 JS, Fujimoto JG, Flammer J, Orgül S, Costa VP, Orzalesi N, Kriegelstein GK, Serra
464 LM, Renard JP, Stefánsson E, Huang D, Swanson EA, Lin CP, Schuman JS, Stinson
465 WG, Chang W, Hee MR, Flotte T, Gregory K, Puliafito CA, Fujimoto JG. Total retinal
466 blood flow measurement with ultrahigh speed swept source/Fourier domain OCT.
467 *Biomed Opt Express*, Vol 2, Issue 6, pp 1539-1552. 2011;2(6):1539-1552.
468 doi:10.1364/BOE.2.001539
- 469 11. Werkmeister RM, Dragostinoff N, Palkovits S, Told R, Boltz A, Leitgeb RA, Gröschl M,
470 Garhöfer G, Schmetterer L. Measurement of Absolute Blood Flow Velocity and Blood
471 Flow in the Human Retina by Dual-Beam Bidirectional Doppler Fourier-Domain
472 Optical Coherence Tomography. *Invest Ophthalmol Vis Sci*. 2012;53(10):6062-6071.
473 doi:10.1167/IOVS.12-9514
- 474 12. Wartak A, Beer F, Desissaire S, Baumann B, Pircher M, Hitzemberger CK.
475 Investigating spontaneous retinal venous pulsation using Doppler optical coherence
476 tomography. *Sci Reports* 2019 91. 2019;9(1):1-11. doi:10.1038/s41598-019-40961-4

- 477 13. Arya M, Rashad R, Sorour O, Moulton EM, Fujimoto JG, Waheed NK. Optical
478 Coherence Tomography Angiography (OCTA) Flow Speed Mapping Technology for
479 Retinal Diseases. *Expert Rev Med Devices*. 2018;15(12):875.
480 doi:10.1080/17434440.2018.1548932
- 481 14. Maloca PM, Feu-Basilio S, Schottenhamml J, Valmaggia P, Scholl HPN, Rosinés-
482 Fonoll J, Marin-Martinez S, Inglin N, Reich M, Lange C, Egan C, Zweifel S, Tufail A,
483 Spaide RF, Zarranz-Ventura J. Reference database of total retinal vessel surface
484 area derived from volume-rendered optical coherence tomography angiography. *Sci*
485 *Rep*. 2022;12(1). doi:10.1038/s41598-022-07439-2
- 486 15. Schmitt JM. Optical Coherence Tomography (OCT): a review. *IEEE J Sel Top*
487 *Quantum Electron*. 1999;5(4):1205-1215. doi:10.1109/2944.796348
- 488 16. Aumann S, Donner S, Fischer J, Müller F. Optical Coherence Tomography (OCT):
489 Principle and Technical Realization. In: *High Resolution Imaging in Microscopy and*
490 *Ophthalmology*. Springer; 2019:59-85. doi:10.1007/978-3-030-16638-0_3
- 491 17. Yaqoob Z, Wu J, Yang C. Spectral domain optical coherence tomography: a better
492 OCT imaging strategy. *Biotechniques*. 2005;39(6 Suppl). doi:10.2144/000112090
- 493 18. Yun SH, Tearney GJ, de Boer JF, Bouma BE. Motion artifacts in optical coherence
494 tomography with frequency-domain ranging. *Opt Express*. 2004;12(13):2977.
495 doi:10.1364/opex.12.002977
- 496 19. Walther J, Mueller G, Morawietz H, Koch E. Signal power decrease due to fringe
497 washout as an extension of the limited Doppler flow measurement range in spectral
498 domain optical coherence tomography. *J Biomed Opt*. 2010;15(4):041511.
499 doi:10.1117/1.3466578
- 500 20. Szkulmowski M, Wojtkowski M, Huang D, Swanson EA, Lin CP, Schuman JS, Stinson
501 WG, Chang W, Hee MR, Flotte T, Gregory K, Puliafito CA, Fujimoto JG, Szkulmowski
502 M, Gorczynska I, Bukowska D, Wojtkowski M, Targowski P. Averaging techniques for
503 OCT imaging. *Opt Express, Vol 21, Issue 8, pp 9757-9773*. 2013;21(8):9757-9773.
504 doi:10.1364/OE.21.009757
- 505 21. Spaide RF, Valmaggia P, Maloca PM, Scholl HPN, Otto TP, Caujolle S. Imaging the
506 vitreous with a novel boosted optical coherence tomography technique: Vitreous
507 degeneration and cisterns. *Retina*. 2022;42(8):1433-1441.
508 doi:10.1097/IAE.0000000000003474
- 509 22. De Boer JF, Leitgeb R, Wojtkowski M, Huang D, Swanson EA, Lin CP, Schuman JS,
510 Stinson WG, Chang W, Hee MR, Flotte T, Gregory K, Puliafito CA, Fujimoto JG.
511 Twenty-five years of optical coherence tomography: the paradigm shift in sensitivity
512 and speed provided by Fourier domain OCT [Invited]. *Biomed Opt Express, Vol 8,*
513 *Issue 7, pp 3248-3280*. 2017;8(7):3248-3280. doi:10.1364/BOE.8.003248
- 514 23. Choma MA, Sarunic M V., Izatt JA, Yang C. Sensitivity advantage of swept source
515 and Fourier domain optical coherence tomography. *Opt Express, Vol 11, Issue 18, pp*
516 *2183-2189*. 2003;11(18):2183-2189. doi:10.1364/OE.11.002183
- 517 24. Thévenaz P, Ruttimann UE, Unser M. A pyramid approach to subpixel registration
518 based on intensity. *IEEE Trans Image Process*. 1998;7(1):27-41.
519 doi:10.1109/83.650848
- 520 25. Sjoberg DD, Whiting K, Curry M, Lavery JA, Larmarange J. Reproducible Summary
521 Tables with the gtsummary Package. *R J*. 2021;13(1):570-580. doi:10.32614/rj-2021-
522 053

- 523 26. Fedorov A, Beichel R, Kalpathy-Cramer J, Finet J, Fillion-Robin JC, Pujol S, Bauer C,
524 Jennings D, Fennessy F, Sonka M, Buatti J, Aylward S, Miller J V., Pieper S, Kikinis
525 R. 3D Slicer as an image computing platform for the Quantitative Imaging Network.
526 *Magn Reson Imaging*. 2012;30(9):1323-1341. doi:10.1016/j.mri.2012.05.001
- 527 27. Jørgensen TM, Thomadsen J, Christensen U, Soliman W, Sander B. Enhancing the
528 signal-to-noise ratio in ophthalmic optical coherence tomography by image
529 registration—method and clinical examples. *J Biomed Opt*. 2007;12(4):041208.
530 doi:10.1117/1.2772879
- 531 28. Spaide RF, Valmaggia P, Maloca PM. IMAGING the VITREOUS with A NOVEL
532 BOOSTED OPTICAL COHERENCE TOMOGRAPHY TECHNIQUE: Posterior
533 Vitreous Detachment. *Retina*. 2022;42(8):1425-1432.
534 doi:10.1097/IAE.0000000000003500
- 535 29. Walther J, Koch E. Flow measurement by using the signal decrease of moving
536 scatterers in spatially encoded Fourier domain optical coherence tomography. In:
537 *Optical Coherence Tomography and Coherence Domain Optical Methods in*
538 *Biomedicine XIII*. Vol 7168. SPIE; 2009:71681S. doi:10.1117/12.808737
- 539 30. Van Velthoven MEJ, Van Der Linden MH, De Smet MD, Faber DJ. Influence of
540 cataract on optical coherence tomography image quality and retinal thickness. *Br J*
541 *Ophthalmol*. 2006;90:1259-1262. doi:10.1136/bjo.2004.097022
- 542 31. Choi W, Moulton EM, Waheed NK, Adhi M, Lee B, Lu CD, De Carlo TE, Jayaraman V,
543 Rosenfeld PJ, Duker JS, Fujimoto JG. Ultrahigh Speed Swept Source OCT
544 Angiography in Non-Exudative Age-Related Macular Degeneration with Geographic
545 Atrophy. *Ophthalmology*. 2015;122(12):2532. doi:10.1016/J.OPHTHA.2015.08.029
- 546 32. Braaf B, Donner S, Uribe-Patarroyo N, Bouma BE, Vakoc BJ. A Neural Network
547 Approach to Quantify Blood Flow from Retinal OCT Intensity Time-Series
548 Measurements. *Sci Rep*. 2020;10(1). doi:10.1038/s41598-020-66158-8
- 549 33. Grieshaber MC, Flammer J. Blood flow in glaucoma. *Curr Opin Ophthalmol*.
550 2005;16(2):79-83. doi:10.1097/01.icu.0000156134.38495.0b
- 551 34. Flammer J, Orgül S, Costa VP, Orzalesi N, Kriegelstein GK, Serra LM, Renard JP,
552 Stefánsson E. The impact of ocular blood flow in glaucoma. *Prog Retin Eye Res*.
553 2002;21(4):359-393. doi:10.1016/S1350-9462(02)00008-3
- 554 35. Schmetterer L, Wolzt M. Ocular blood flow and associated functional deviations in
555 diabetic retinopathy. *Diabetologia*. 1999;42(4):387-405. doi:10.1007/s001250051171
- 556 36. Gurovich AN, Braith RW. Pulse wave analysis and pulse wave velocity techniques:
557 Are they ready for the clinic. *Hypertens Res*. 2011;34(2):166-169.
558 doi:10.1038/hr.2010.217
- 559 37. Levy JH, Kouz K, Scheeren TWL, De Backer D, Saugel B. ClinicaL FoCUS Review
560 Pulse Wave Analysis to Estimate Cardiac Output. *Anesthesiology*. 2021;134:119-145.
561 doi:10.1097/ALN.0000000000003553
- 562 38. Jin Y, Wang X, Irnadiastputri SFR, Mohan RE, Aung T, Perera SA, Boote C, Jonas
563 JB, Schmetterer L, Girard MJA. Effect of changing heart rate on the ocular pulse and
564 dynamic biomechanical behavior of the optic nerve head. *Investig Ophthalmol Vis Sci*.
565 2020;61(4):27-27. doi:10.1167/iovs.61.4.27

566

567

568 **Tables**

569 **Table 1.** Vessel–RNFL comparison of SNR

570

Variable	20 kHz, N = 78	40 kHz, N = 132	85 kHz, N = 228	125 kHz, N = 351
SNR_{B-scan} [dB]	39.7 (38.9, 40.6)	37.8 (37.3, 38.5)	36.0 (35.0, 36.9)	32.6 (31.7, 33.8)
SNR_{Subvolume} [dB]				
Artery	6.8 (2.6, 8.7)	5.3 (2.1, 8.5)	11.8 (6.2, 15.4)	12.7 (10.0, 15.2)
RNFL	33.7 (32.4, 34.6)	32.2 (31.1, 33.4)	30.7 (29.7, 31.6)	28.7 (27.4, 29.6)
Noise Level [RAW value]	55,186 (51,028, 61,463)	110,620 (94,717, 124,661)	202,044 (179,693, 228,765)	146,278 (129,426, 165,785)
SNR_{Subvolume} / Peak SNR_{Subvolume} [%]				
Artery	4.68 (1.89, 7.09)	2.76 (1.32, 5.79)	1.40 (0.39, 3.27)	2.23 (1.19, 3.96)
RNFL	14.2 (10.7, 17.6)	17.3 (13.3, 22.3)	13.8 (10.9, 17.0)	13.9 (10.5, 17.0)
SNR_{Subvolume} / SNR_{B-scan} [%]				
Artery	0.05 (0.02, 0.07)	0.06 (0.03, 0.11)	0.38 (0.13, 0.73)	1.10 (0.58, 1.64)
RNFL	24 (16, 30)	27 (22, 34)	28 (24, 33)	42 (31, 48)

Results are presented as median (IQR)

571 RNFL: retinal nerve fibre layer, N: number of B-scans with matched vessel-RNFL annotations, SNR: signal-to-
 572 noise ratio, SNR_{B-scan}: SNR in the complete B-scan, SNR_{Subvolume}: SNR in the B-scan subvolume, RAW value:
 573 value extracted from the raw .vol OCT files, Peak SNR_{Subvolume}: maximal SNR on a pixel level in the complete
 574 subvolume over time, IQR: interquartile range.

575 **Table 2.** Acquisition overview per nominal A-scan rate

	20 kHz, N = 109	40 kHz, N = 113	85 kHz, N = 122	125 kHz, N = 122
B-scan Interval [ms]	49 (49, 49)	25 (25, 25)	13 (13, 13)	9 (9, 9)
Exam Duration [ms]	4,224 (3,528, 5,317)	4,042 (3,582, 4,376)	3,411 (2,950, 3,759)	2,867 (2,059, 3,321)
Annotated B-scans per Image Stack [n]	86 (72, 108)	159 (141, 172)	253 (219, 279)	303 (218, 351)
SNR_{B-scan} [dB]	39.8 (37.3, 42.4)	38.0 (35.3, 39.6)	34.6 (31.0, 36.0)	32.2 (29.9, 34.4)
Peak B-scan Intensity [RAW value]	555,997,151 (340,536,329, 1,034,710,323)	786,543,813 (345,832,675, 1,310,379,806)	685,001,499 (347,938,689, 963,279,206)	239,018,674 (168,368,268, 488,855,979)
Annotated Image Stacks [N]				
Optic nerve head centre	9 (8.3%)	13 (12%)	13 (11%)	13 (11%)
NRM	38 (35%)	31 (27%)	42 (34%)	42 (34%)
1 ODD from NRM	16 (15%)	17 (15%)	17 (14%)	17 (14%)
2 ODDs from NRM	14 (13%)	19 (17%)	17 (14%)	17 (14%)
3 ODDs from NRM	17 (16%)	17 (15%)	17 (14%)	17 (14%)
4 ODDs from NRM	12 (11%)	13 (12%)	13 (11%)	13 (11%)
5 ODDs from NRM	3 (2.8%)	3 (2.7%)	3 (2.5%)	3 (2.5%)

Results are presented as median (IQR) of the average values per image stack | N (% of image stacks per acquisition rate)

576 N: number of time-resolved image stacks, SNR_{B-scan}: signal-to-noise ratio in the complete B-scan; RAW value:

577 value extracted from the raw .vol OCT files; NRM: Neuroretinal rim, 1 ODD from NRM: eccentricity of 1 optic disc

578 diameter from the neuroretinal rim, IQR: interquartile range.

579 **Table 3.** Vessel subvolume SNRs and calculated velocities

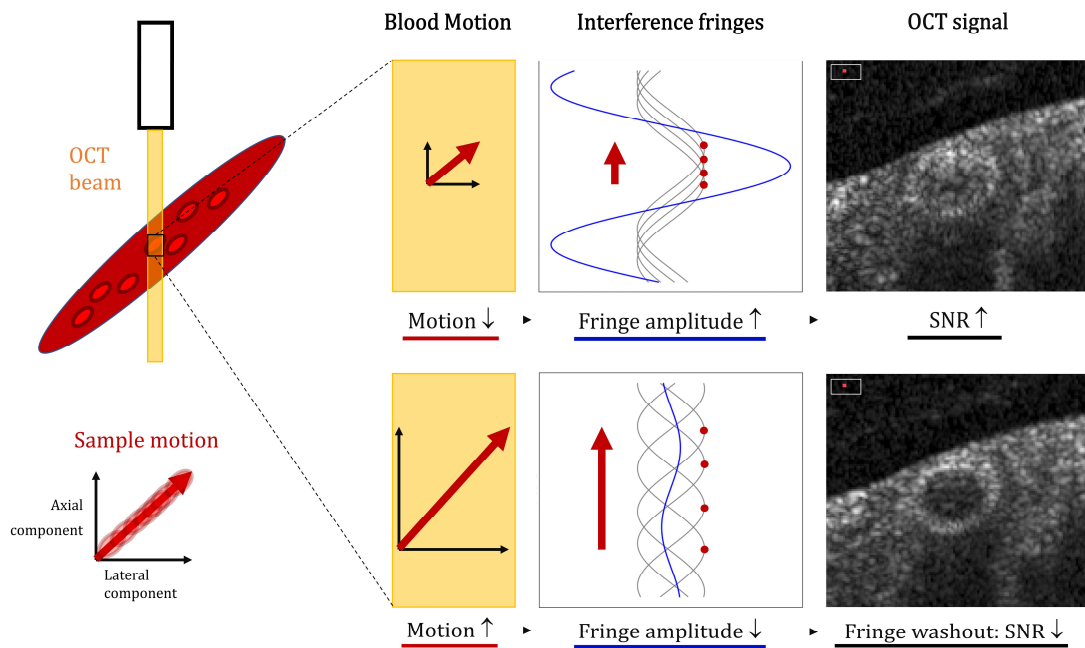
580

Variable	20 kHz, N = 109	40 kHz, N = 113	85 kHz, N = 122	125 kHz, N = 122
SNR_{Vessel} [unitless]	400 (134, 995)	328 (151, 610)	159 (75, 312)	105 (50, 201)
Vessel Intensity [RAW value]	25,043,042 (7,035,096, 62,483,917)	42,599,201 (17,286,374, 73,869,286)	36,436,880 (16,508,790, 69,969,934)	15,610,795 (7,235,353, 30,854,052)
SNR_{Vessel} / Peak SNR_{Vessel} [%]	5.7 (4.6, 6.9)	5.4 (3.8, 6.9)	5.3 (3.8, 7.0)	5.0 (3.9, 6.6)
Average Velocity [a.u.]	7 (6, 8)	14 (12, 16)	29 (26, 33)	43 (38, 48)
Minimal Velocity [a.u.]	5 (5, 5)	11 (10, 11)	22 (22, 23)	33 (32, 34)
Maximal Velocity [a.u.]	8 (7, 10)	17 (14, 21)	35 (29, 44)	53 (43, 62)

Results are presented as median (IQR) of the average values per image stack

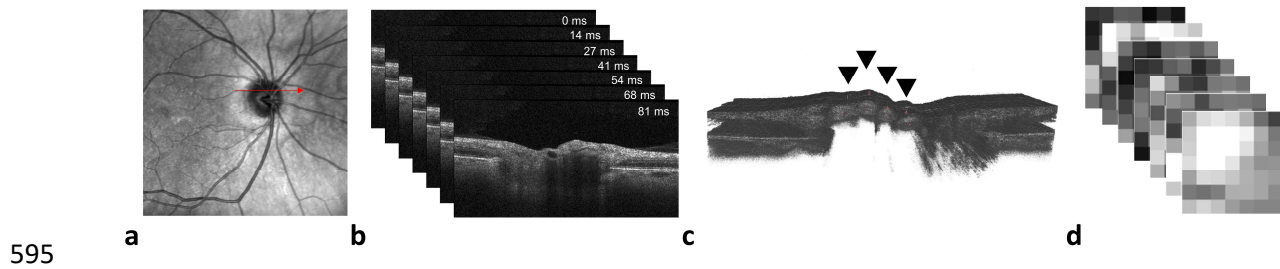
581 N: number of time-resolved image stacks, SNR: signal-to-noise ratio, SNR_{Vessel}: Average SNR in the vessel
582 subvolumes of the B-Scan, RAW value: value extracted from the raw .vol OCT files, Peak SNR_{Vessel}: maximal
583 SNR on a pixel level in the complete vessel subvolume over time, Average Velocity: average of the numerical
584 solutions to the SNR_{Drop} equation per B-scan, Minimal Velocity: smallest numerical solution, Maximal Velocity:
585 largest numerical solution, a.u.: arbitrary unit, IQR: interquartile range.

586 **Figures**

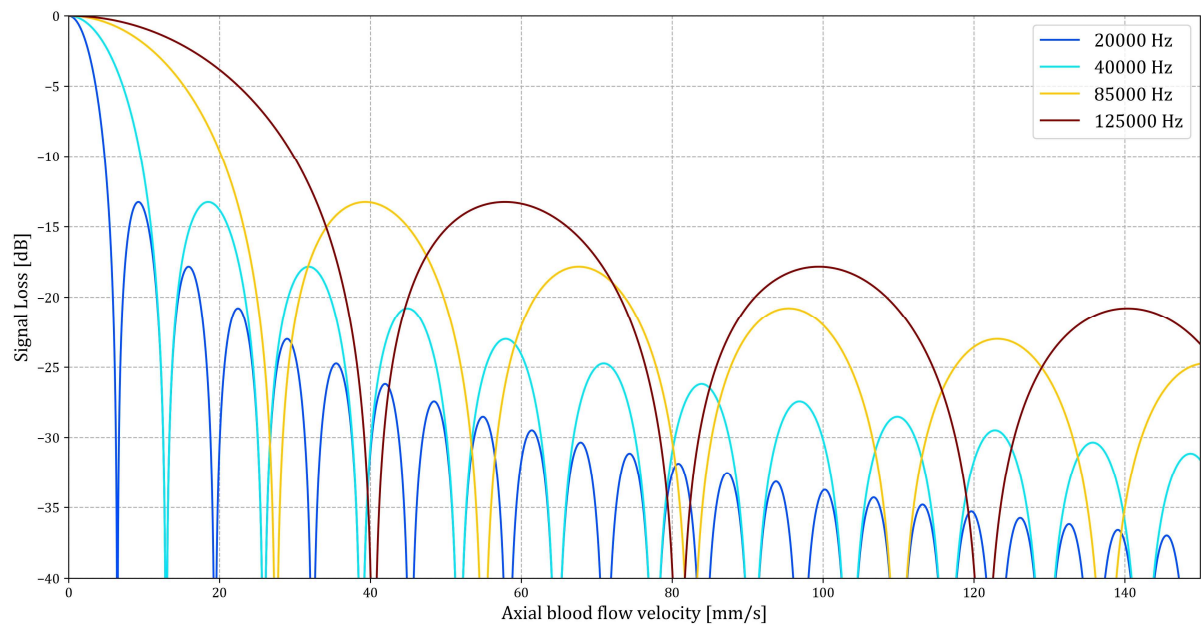


587

588 **Figure 1.** Illustration of the fringe washout in spectral-domain optical coherence tomography (OCT). Fringe
589 washout describes the signal drop in the OCT when the sample moves through the sample beam during
590 illumination. The sample motion can be split into two components: a lateral component and an axial component.
591 When the integration time is shorter or the velocity is smaller, there is less motion, the fringe amplitude is higher
592 and, hence, the OCT intensity is higher. When the integration time is longer or the velocity is higher, the sample
593 has a larger motion, which leads to a lower fringe amplitude. This fringe washout causes a higher SNR drop and
594 a lower OCT intensity (bottom right).



596 **Figure 2.** Time-resolved dynamic optical coherence tomography-based extraction of vessel subvolumes. **a**
597 Scanning laser ophthalmoscopy (SLO) image. The red arrow indicates the position of the continuous
598 acquisitions, which can be started by a press on the joystick. **b** The time-resolved B-scans are continuously
599 acquired with a time stamp for each B-scan. **c** The continuous images are registered and reconstructed as a
600 three-dimensional volume, where the third dimension represents the time axis. On each B-scan, the vessel
601 centres were manually annotated. **d** Subvolumes of 7×7 pixels surrounding the vessel centre were extracted
602 and further processed for fringe washout analysis.



603

604

Figure 3. Axial blood flow velocity component calculation. The axial blood flow velocity is calculated at SNR

605

drops for the four nominal acquisition rates of 20, 40, 85 and 125 kHz. As seen, several potential axial blood flow

606

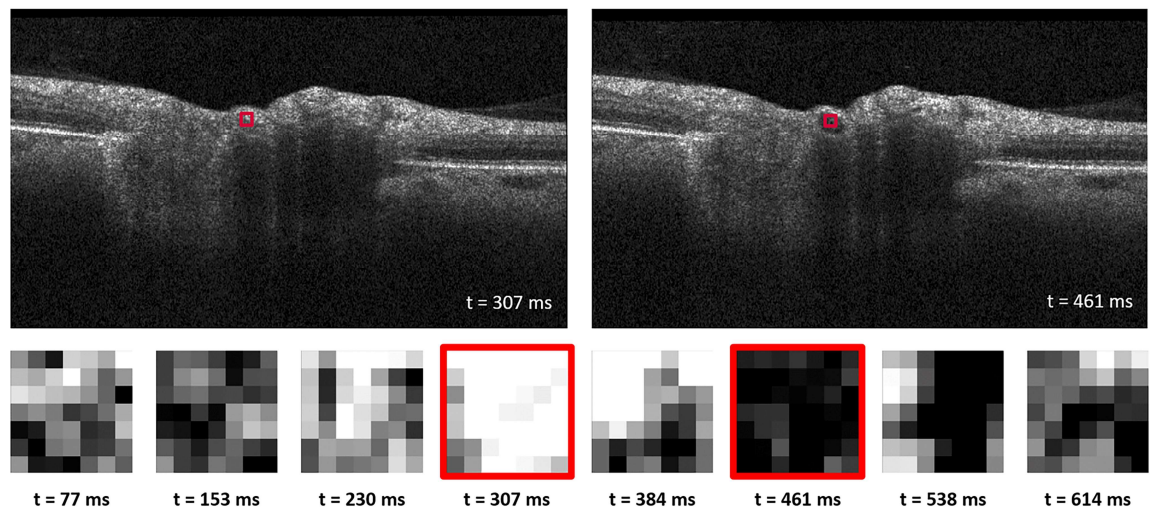
velocities are based on a single signal-to-noise ratio (SNR) drop. The numerical solutions to the equation were

607

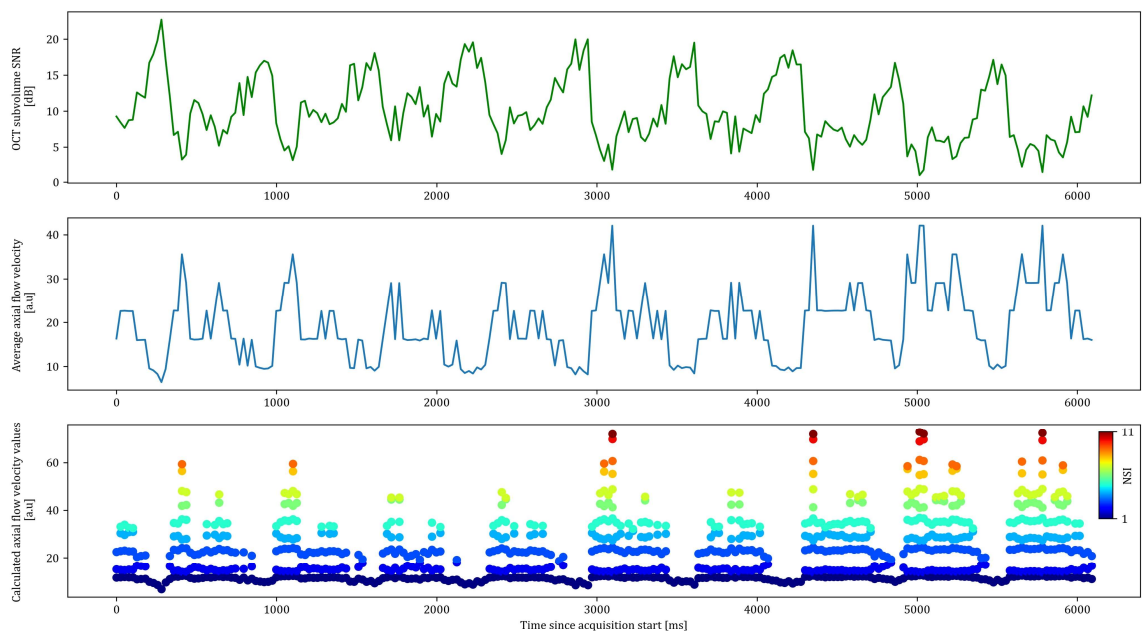
used to generate the blood flow profiles in the time-resolved dynamic OCT acquisitions. The values here

608

represent the calculated velocities in mm/s, where the SNR drop is compared against a known reference SNR.



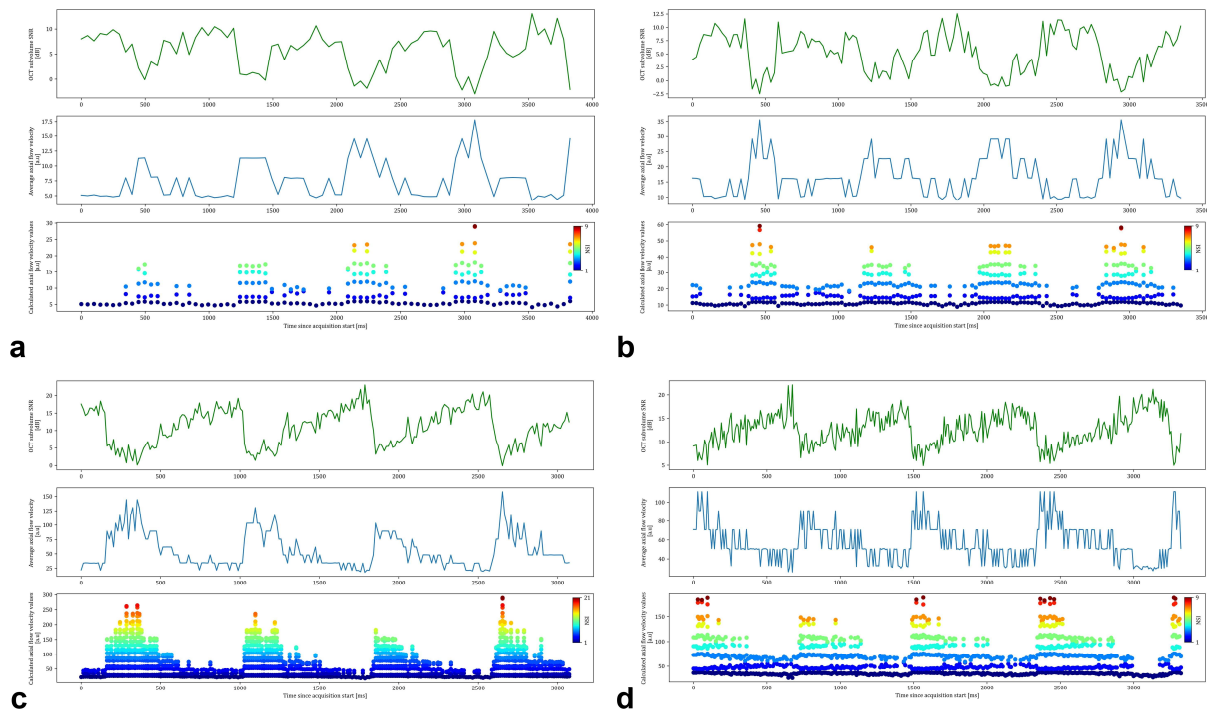
a



b

609

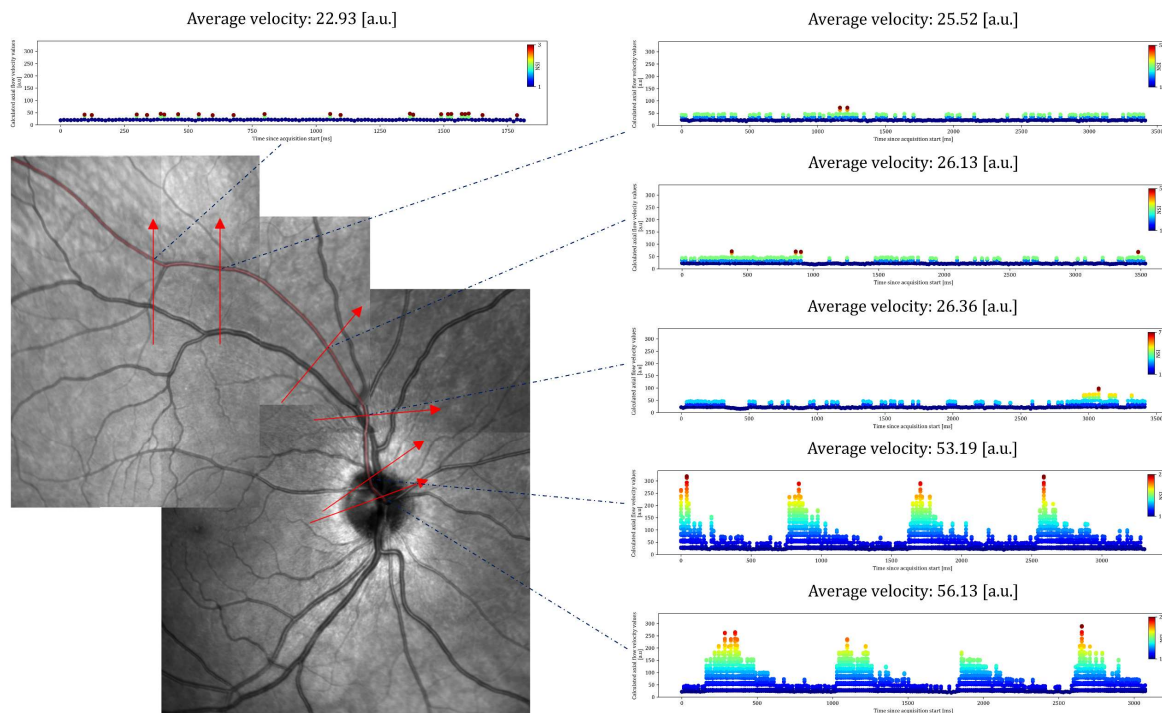
610 **Figure 4.** Time-resolved optical coherence tomography (OCT) B-scans of optic nerve head vessels. **a** Imaging
 611 was performed at the same location. Two B-scans and eight extracted 7×7 pixel arterial subvolumes ($20 \times$
 612 $27 \mu\text{m}$) are shown with timestamps. The corresponding subvolumes are framed in red, where the red frame on
 613 the original B-scan is enlarged for better visualisation. The intensity changes in the subvolume occur due to
 614 varying fringe washout of the arterial signal over time. **b** Analysis of retinal blood flow dynamics over 6 s in an
 615 artery with time-resolved OCT (A-scan integration time of $22.4 \mu\text{s}$, inter-B-scan interval of ~ 25 ms). Timestamp-
 616 matched mean SNR of the OCT subvolume (top row), average axial flow velocity (middle row) and calculated
 617 axial flow velocity values (bottom row) are presented. The average axial flow velocity line (middle row) represents
 618 the average of the numerical solutions, and the dots (bottom row) represent all numerical solutions to the SNR_{Drop}
 619 equation. dB: decibel, a.u.: arbitrary unit, NSI: numerical solution index.



620

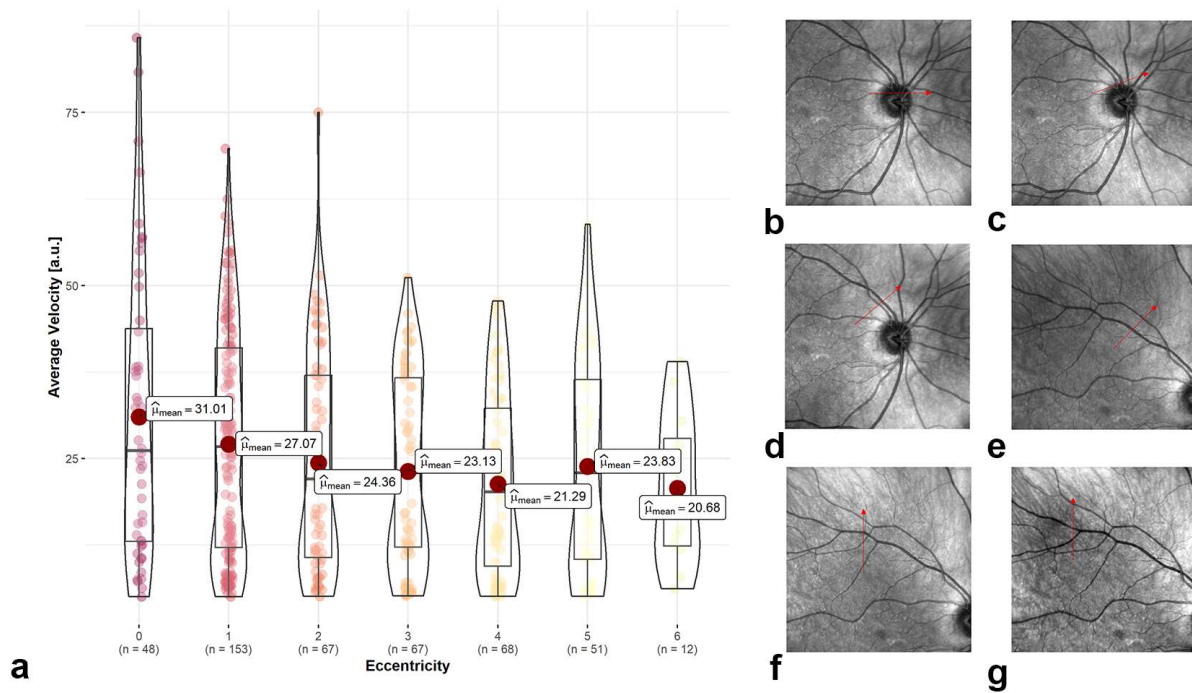
621 **Figure 5.** Calculated flow velocity profiles of time-resolved OCT intensity at the four different nominal acquisition
622 rates (a 20 kHz, b 40 kHz, c 85 kHz and d 125 kHz). Each subfigure shows the acquisition duration in ms from
623 the start on the x-axis. On the y-axes, the mean OCT SNR from the subvolume can be found on the top row, the
624 average flow velocity (average of the numerical solutions to the SNR_{Drop} equation) in blue on the middle row and
625 the calculated flow profiles (all numerical solutions) as dots on the bottom row.

626



627

628 **Figure 6.** En-face representation of time-resolved acquisitions along an artery. The montage scanning laser
629 ophthalmoscopy (SLO) of different acquisitions in the bottom left indicates the OCT acquisition locations as
630 arrows, and the analysed artery is presented in transparent red. The corresponding time-resolved dynamic blood
631 flow profiles show a clear pulsatility close to the optic nerve head centre, which diminishes beyond the optic
632 nerve head rim. The estimated average blood flow velocities decrease from the optic nerve head centre towards
633 the periphery.



634

635 **Figure 7. a** Estimated average blood flow velocity of the measured vessels at different eccentricities represented
 636 as violin-boxplots and with the means highlighted as red dots. **b–g** Example scanning laser ophthalmoscopy
 637 (SLO) acquisitions with the positioning of the continuous B-scans highlighted by a red arrow corresponding to
 638 eccentricities 0–5. **b** \triangleq 0: Optic nerve head centre, **c** \triangleq 1: Neuroretinal rim, **d** \triangleq 2: eccentricity of 1 optic disc
 639 diameter (ODD) from the neuroretinal rim, **e** \triangleq 3: eccentricity of 2 ODDs from the neuroretinal rim, **f** \triangleq 4:
 640 eccentricity of 3 ODDs from the neuroretinal rim, **g** \triangleq 5: eccentricity of 4 ODDs from the neuroretinal rim.

641 **Supplementary Material**

642 **Supplementary Video 1**

643 Time-resolved dynamic optical coherence tomography of an artery (cross-sectional)
644 at the centre of the optic nerve head.

645

646 **Supplementary Video 2**

647 Time-resolved dynamic optical coherence tomography of an artery (longitudinal) at
648 the centre of the optic nerve head.

649

650 **Supplementary Video 3**

651 Comparison of time-resolved dynamic optical coherence tomography with
652 corresponding blood flow velocity profiles at four different integration times.